Mechanical Enhancement of Graded Nanoporous Structure

Lijie He
Materials Science Program,
University of Rochester,
Rochester, NY 14611
e-mail: lhe5@ur.rochester.edu

Niaz Abdolrahim
Materials Science Program;
Department of Mechanical Engineering,
University of Rochester,
Rochester, NY 14611
e-mail: niaz@rochester.edu

Inspired by the development of strong and ductile composite and gradient materials over the past decade, here, we report the investigation of a graded nanoporous (NP) structure utilizing molecular dynamics simulations. The structure is generated by inducing a gradient scaling parameter in a Gaussian random field model. It has a large ligament/pore size toward the core and a small ligament/pore size toward the surface. The redistribution of stress and strain under tensile loading is then scrutinized and compared between the functional graded NP structure and two conventional NP structures with identical relative density but constant ligament size. During loading, the thick ligaments in the gradient structure yield at high stress, leading to the entire structure's high mechanical strength. The thin ligaments help the structure accommodate significant plastic strain by promoting uniform deformation. Both parts of the gradient structure worked collectively and resulted in the structure exhibiting a synergy of excellent strength and good deformability.
[DOI: 10.1115/1.4051470]

Keywords: elastic behavior, fracture, mechanical behavior, microstructure property relationships, plastic behavior

1 Introduction

Nanoporous (NP) metals are bicontinuous three-dimensional structures with ligaments and pores. Their unique microstructures with tortuous surfaces give rise to an excellent surface-to-volume ratio, making them great candidates for various applications such as electrochemical sensors/actuators [1–4], fuel cell filters [5], and catalysts [1]. However, it is well known that albite the individual ligaments in NP metals have excellent ductility; the NP metals as a whole often break in a brittle manner under tensile loading [6–10]. Biener et al. [6,11] and Hodge et al. [12] have attributed this phenomenon to the narrow ligaments size distribution. Overall, this brittle nature of NP metal could be a hindrance in many applications [8,11,13]. Numerous studies [7,14,15] have shown that unlike their microscopic counterparts, the mechanical properties of NP metals are affected by not only their relative density but also their ligament size—the considerable surface energy and subsequential dislocation density play an essential role in the deformation. Thus, it is often suggested to combat the loss of ductility by fine-tuning the aforementioned morphological properties directly. For example, using atomistic simulations, To et al. [16] demonstrated that increasing porosity enhances deformability. Nevertheless, the enhancement through adjusting a single morphological parameter is often accompanied by the loss of strength [11] and stiffness [12], making it compelling to look into alternative strategies. One possible method will be adding a shell layer onto the nanoporous core and form into a heterostructured architecture, which we explored in detail in our previous paper [17]. The induced core–shell interface in such architecture hinders dislocation movement and promotes sessile dislocation and twinning nucleation, which alleviated strain localization and improved deformability.

Another possible strategy will be constructing a gradient NP structure. Gradient materials are an emerging class of bio-inspired materials [18–20] proven to possess remarkable and superior mechanical properties [21–23]. Van der Stok et al. [24] demonstrated that a gradient in structural cell size significantly influenced bone ingrowth and implant fixation ability. Li et al. [25] have published a detailed review paper on the mechanical properties and deformation mechanisms in various gradient structures, including gradient nano-grained, nano-laminated, and nanotwinned structures. These structures possess a spatial gradient in their microstructures and often exhibit extraordinary strength-ductility synergy, which is absent in their non-gradient counterparts. Liu et al. [26] have successfully designed and synthesized functionally graded porous scaffolds with gyroid/diamond unit cells and gradient in cell size, which achieved great strength and elastic modulus. Wang et al. [27] conducted a finite element method study and revealed that polycrystalline structures with a gradient in grain size possess enhanced strength without ductility reduction. The mechanical enhancement of gradient structures could originate from multiple mechanisms, from plastic strain gradient strengthening [28] to unique dislocation structures strengthening, such as geometrically necessary dislocation strengthening and sessile dislocation strengthening [29,30]. All these studies demonstrated that when mechanical performance is related to specific morphological properties, introducing a spatial gradient into these properties could result in unprecedented performance. As for NP structure, it is well known that ligament size has a significant effect on both the elastic properties and plastic properties due to multiple reasons, such as suppressed nucleation, emission as well as reabsorption of dislocations by free surfaces [7], changing of deformation mode [14], and redistribution capability of the overloading stress [16]. Merely adjusting the ligament size to larger or smaller only achieves a trade-off between strength and deformability. Thus, it is hypothesized that generating an NP structure with a gradient in ligament size could potentially achieve unprecedented strength and deformability.

In this paper, a three-dimensional (3D) NP structure model with a gradient in ligament size is employed to explore the gradient effect in nanoporous materials. Experiments performed by Biener et al. [6,11] and Hodge et al. [12] have already established that ligament size has an enormous impact on the elastic properties of NP materials. The study by To et al. [16] has also shown that ligament size is relevant to surface area and redistribution of stress, which govern the plasticity performance of the structure. Hence, we hypothesize that NP gradient structure could benefit from the presence of both large and small ligaments and exhibit unprecedented mechanical properties. The 3D NP gradient structure is generated for the first time by introducing morphological scaling parameters into the leveled-wave model developed by Cahn [31] and

Contributed by the Materials Division of ASME for publication in the Journal of Engineering Materials and Technology. Manuscript received January 30, 2021; final manuscript received June 7, 2021; published online June 23, 2021. Assoc. Editor: Tariq Khraishi.

Soyarslan et al. [32]. Its mechanical properties and deformation mechanisms are investigated under tensile loading using the molecular dynamics (MD) method and then compared with two conventional NP models with constant ligament size. As a result, the NP gradient structure exhibits a synergy of high strength and good deformability.

2 Methods

2.1 Gaussian Random Field Model and Cell-Size Gradient Introduction. In this study, we generated three NP structures made of copper: two with constant ligament size (2.8 nm and 11.2 nm) and one with gradient ligament size (2.8 nm to 11.2 nm). All three structures have the same relative density of 45% and are connected to a top and a bottom substrate (5.4 nm thick each) of the same material. Details on the connection between the nanoporous part and the substrate are illustrated later in this section. Cross-section examples of the structures are shown in Fig. 1. The nanoporous part of each NP metal is generated through a two-step process. First, we utilize the leveled-wave model developed by Cahn [31] and Soyarslan et al. [32] to obtain a structure's volume mesh. Second, we superposition this volume mesh with a perfect single crystalline copper structure with a size of 108.45 nm × 36.15 nm × 46.15 nm, and we curve out all pores, leaving only the ligament network. The resulting models from the leveled-wave method are known to show great accuracy compared to experimental structures and conventional mathematical models generated by the Monte Carlo method and the phase-field method [32]. This level wave model comprises a series of standing sinusoidal waves satisfying specific conditions: they must have the same fixed wavelengths and random spatial directions and phases. These waves can be expressed as follows:

$$f(x, y, z) = \sqrt{\frac{2}{N}} \sum_{i=1}^{N} \cos(\alpha q_{ix} x + \beta q_{iy} y + \gamma q_{iz} z + \varphi_i) \tag{1}$$

where (x, y, z) is the location vector, N is the total number of waves (N should be sufficiently large to ensure randomness in the structure, we used $N = 10{,}000$ in this study), $\sqrt{2/N}$ is the normalization vector, (q_{ix}, q_{iy}, q_{iz}) and φ_i denotes the wave direction and wave phase of the ith wave. The wavenumber is chosen to be constant as $|(q_{ix}, q_{iy}, q_{iz})| = q_0$ so all waves have the same wavelength. Wave direction uniformly distributed over the solid angle 4π, and wave phase uniformly distributed over an interval from 0 to 2π. Different phases in the system will then be determined by a level cut value ξ

$$\begin{aligned} &\text{point } (x, y, z) \text{ locates in the solid phase if } f(x, y, z) < \xi \\ &\text{point } (x, y, z) \text{ locates on the pore-solid surface if } f(x, y, z) = \xi \\ &\text{point } (x, y, z) \text{ locates in the pore phase if } f(x, y, z) > \xi \end{aligned} \tag{2}$$

The level cut value is known to be closely related to relative density. In this study, ξ is tailored to ensure the relative density is 45% for most of the porous part of the structures (36.15 nm in thickness along the z-direction, as illustrated in Fig. 1(*a*)). The porous part of the structures is connected to the top and bottom substrates (5.4 nm in thickness for each substrate) through two transit zones (5 nm in thickness for each transit zone). In the transit zones, ξ increases from 45% to 100% linearly. The introduction of the transit zones is to ensure the porous part is smoothly connected to the solid substrate and avoid the presence of any sharp angle at the connecting interfaces. Then, all enclosed pores in the transit zones are filled to ensure the structure is bicontinuous.

The α, β, and γ are morphological scaling parameters related to ligament thickness in x, y, and z directions, respectively. By expressing these scaling parameters as functions of the location vector, we can effectively control the ligament size and even introduce a spatial size gradient into the structure. In order to keep the structure surface change smoothly and avoid shape distortion across all dimensions, the morphological scaling parameters have to satisfy the following relation:

$$\frac{d(\alpha \cdot x)}{dx} = \frac{d(\beta \cdot y)}{dy} = \frac{d(\gamma \cdot z)}{dz} \tag{3}$$

Structures are subsequentially generated for this study by employing different scaling parameters. We generated two structures with constant ligament size, shown as realization $c1$ (average ligament size of 2.8 nm) and $c2$ (average ligament size of 11.2 nm) in Figs. 1(*a*) and 1(*b*) using the following scaling parameters:

$$\alpha_{c1} = \beta_{c1} = \gamma_{c1} = 1 \tag{4a}$$

$$\alpha_{c2} = \beta_{c2} = \gamma_{c2} = 0.25 \tag{4b}$$

and one structure with a Parabola shape size gradient along the x-direction, which has thick ligaments (average ligament size of 11.2 nm) near the center and thin ligaments (average ligament size of 2.8 nm) near the surfaces, shown as realization $g1$ in

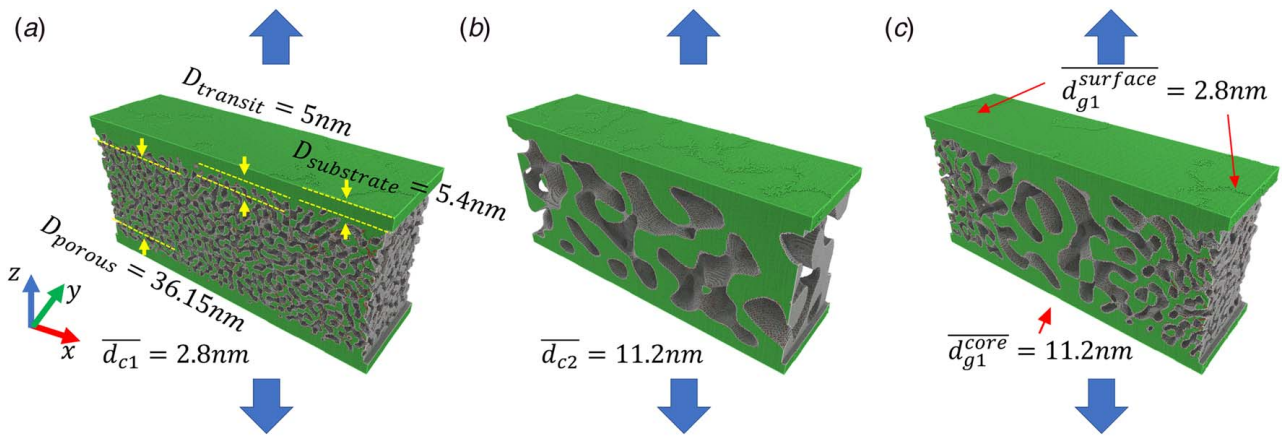

Fig. 1 Snapshots of the cross sections of (*a*) realization *c*1 with an average ligament size of 2.8 nm, (*b*) realization *c*2 with an average ligament size 11.2 nm, and (c) realization *g*1 with a gradient in ligament size from 2.8 nm to 11.2 nm along the *x*-direction. All snapshots are taken after relaxation and before loading. The dimensions of the structures are 108.45 nm × 36.15 nm × 56.95 nm, which includes a 46.15 nm thick porous part and two 5.4 nm thick substrates. Arrows denotes the loading direction (i.e., z-direction).

Fig. 1(*c*). The scaling parameter is calculated as follows:

$$\beta_{g1} = \gamma_{g1} = k_{g1}(x - x_{center})^2 + C_{g1} \tag{5}$$

where $x_{center} = \dfrac{x_{\max} - x_{\min}}{2}$, $k_{g1} = \dfrac{1 - 0.25}{x_{\max} - x_{center}}$, $C_{g1} = 0.25$.

According to Eqs. (3) and (5), a differential equation can be derived as

$$\dot{\alpha}_{g1}\frac{\alpha_{g1}}{x} = \frac{k_{g1}(x - x_{center})^2 + C_{g1}}{x} \tag{6}$$

solving which will yield α_{g1} in the following form:

$$\alpha_{g1} = \frac{k_{g1} \cdot x^2}{3} - k_{g1}x_{center}x + k_{g1}x_{center}^2 + C_{g1} - k_{g1}x_{center}^3/(3x) \tag{7}$$

Realization *c*1 and *c*2 have constant average ligament sizes of 2.8 nm and 11.2 nm. As shown in Fig. 1, the ligament size is inversely proportional to their respective scaling parameter α_{c1}, β_{c1} and α_{c2}, β_{c2}. In comparison, realization *g*1 has a parabola shape size gradient from 2.8 nm (close to the surface) to 11.2 nm (close to the core) along the *x*-direction. Note that in non-gradient NP structures, periodic boundaries can be generated by choosing specific standing sinusoidal waves with translational periodicity [32]. However, this condition cannot be satisfied when the morphological scaling parameter is position dependent—such as in this study where the ligament size is continuously changing along the *x*-direction. Thus, we choose to construct a structure with free surfaces in the transverse direction and substrates along the loading direction. The free surfaces along the transverse direction are "cut" abruptly, and sharp edges with very high energy are formed. The total length of the sharp edges is longer in structures *c*1 and *g*1 because they have thinner ligaments close to the surface. After energy relaxation, these sharp edges caused higher dislocation density close to the surface compared to the center, and this is more evident in *c*1 and *g*1, as will be seen in Sec. 3.3. As indicated by the arrows in Fig. 1, the loading direction is chosen to be perpendicular to the gradient direction to investigate the complementary effects of domains with different ligament thicknesses and varying plasticity mechanisms. This loading scheme has also been utilized in studies of gradient polycrystal nanograins [27], where stronger grains carry more load while ductile ones share more deformation, thus leading to enhanced strength at no reduction in ductility.

2.2 Molecular Dynamics Simulations. The MD loading of the structures was carried out using LAMMPS [33]. A widely utilized embedded-atom method (EAM) potential developed by Mishin [34] was used to characterize the interaction force between the copper atoms. Many studies have employed this potential to investigate the deformation mechanisms of NP materials made of Cu and Cu alloys [17,35–38]. All three realizations are subjected to the same procedures in the following orders: (1) Energy minimization is performed using the conjugate gradient method with a maximum force tolerance of 10^{-27} eV/A. (2) Thermal relaxation under Noose Hoover isothermal-isobaric (NPT) at 300 K for 200 ps, and (3) uniaxial tensile loading with an average strain rate of 10^9/s at 300 K under the Noose Hoover NPT ensemble. The periodic boundary condition is maintained along the loading direction (z-direction), and free surfaces are applied along both transverse directions. A stepwise loading is adopted to avoid non-equilibrium physics, where the structures are relaxed for 1 ps after each loading step (0.1% strain increment in 1 fs). At any specific external strain, macroscopic stress is determined as the average of the sum of atomic stress during the last 100 fs of the relaxation period following each loading step. Ovito [39] is used for visualization. Polyhedron template matching (PTM) [40] is employed to classify different crystal structures, such as face-centered cubic (FCC), hexagonal closest packed (HCP), and body-centered cubic (BCC). The dislocation analysis tool (DXA) [41] is used to identify different dislocation types and quantify their densities.

3 Result and Discussion

3.1 Stress–Strain Curve. The stress–strain curves of all realizations are shown in Fig. 2(*a*). It can be seen that *c*2 has the largest elastic modulus at 16.24 GPa, *g*1 has a slightly lower elastic modulus at 14.48 GPa, and *c*1 has a significantly lower elastic modulus at 9.33 GPa. Figure 2(*b*) shows the strain hardening rate $\Theta = d\sigma_T/d\varepsilon_T$ of all three structures, where σ_T and ε_T denote the true stress and strain, respectively. Hart [42], Hutchinson and Neale [43], and Yasnikov [44] had developed a criterion that is often used to describe the onset of plastic instability as

$$\Theta \le \sigma_T(1 - m) \tag{8}$$

where *m* is the strain-rate sensitivity parameter for materials. When the materials in consideration are strain-rate independent ($m \approx 0$), such as in this study, Eq. (8) will be reduced to the $\Theta \le \sigma$, known as the Considère criterion of necking [44]. Based on Hart's criterion, having a high work-hardening rate will delay the destabilization of structural integrity and maintain good ductility [25,45]. As shown in Fig. 2(*b*), the strain hardening rate of *c*1 declines slowly as the structure is strained. In contrast, the strain hardening rate for *c*2 declines much faster. As for *g*1, the initial strain hardening rate is comparable with that of the *c*2, but it declines at a reduced rate. Due to high stress and low strain hardening rate, *c*2 is the first structure to develop necking according to the Considère criterion. It is also observed when the strain hardening rate reaches a plateau, *c*1 has the highest strain hardening rate, *c*2 has the lowest strain hardening rate, and *g*1 has a strain hardening rate that is in between. This observation suggests that even during the mid to late stage of the deformation, *g*1 exhibits better deformability than *c*2.

3.2 Atomistic Deformation Behavior. Figure 3 shows the snapshots of *c*1, *c*2, and *g*1 at 0% and 9% strain. The FCC atoms are colored in green, surface atoms are white, and HCP atoms, which are stacking faults between leading and trailing partials, are colored in red. These figures illustrate the detailed plastic deformation mechanism in different structures. Comparing Figs. 3(*a*)–3(*c*), it can be found that when there is no presence of external strain, thin ligaments in *c*1 and *g*1 exhibit a decent amount of stacking faults (i.e., red atoms), while large ligaments in *c*2 and *g*1 are nearly stacking fault free. The relationship between the stacking fault density, dislocation density, ligament size, and surface energy will be further discussed in Sec. 3.3.

When under tensile stress, destabilizing plastic deformation phenomenon such as necking and crack can be observed in all three realizations, as shown in Figs. 3(*d*)–3(*f*). Here, we address the atomistic plastic response of each one of them as follows:

(a) In *c*1, micro neckings/cracks can be seen to have developed in multiple places at 9% strain. These microcracks are small and remote from each other, as indicated by the circles. The reason behind this is the massive number of ligaments presented in the structure. The excessive amount of ligament ensures that weak ligament which would serve as initial necking points is abundant and scattered around in the structure. Upon loading, these weak ligaments succumb to the strain and micro neckings/cracks with limited length are observed across the structure, but few of them would connect and form into large cracks, which would lead to failure. Also, *c*1 exhibits a significant number of sessile dislocations, which further prevent mobile dislocation movement and further necking. Thus, a comparatively uniform plastic deformation is achieved at the macroscopic scale.

(b) In *c*2, more localized neckings are observed at 9% strain. As indicated by the arrows, three necking ligaments are in close

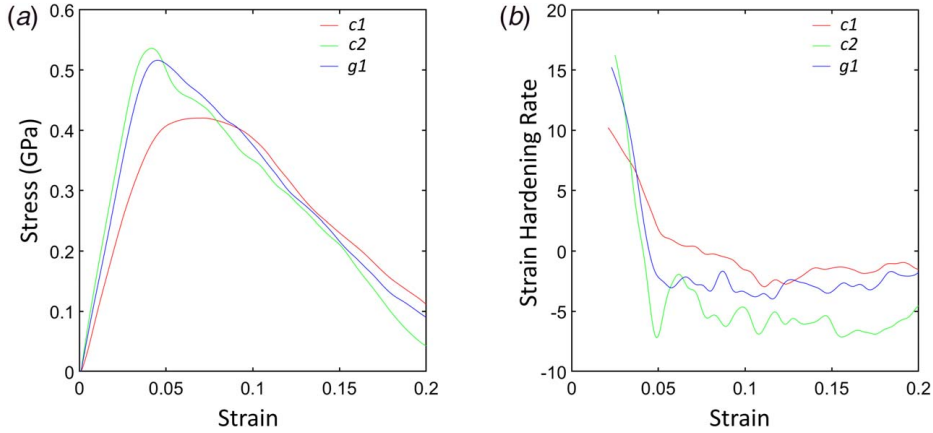

Fig. 2 (*a*) Stress–strain response of all realizations during tensile loading and (*b*) strain hardening rate of all realizations during tensile loading

vicinity to each other in the same horizontal plane. Due to having much fewer ligaments, the necking of any ligament will be accompanied by stress intensification in its vicinity, which subsequentially overloads its neighboring ligaments and leads to a chain reaction of necking formation. These neckings will further aggravate stress concentration in the neighborhood and eventually evolve into large cracking openings. This localized plasticity would greatly hinder the plastic deformability of the structure.

(c) In $g1$, similarly unstable neckings are also observed in the thicker ligaments closer to the core. However, the thinner ligaments closer to the surface are resilient to be affected by the neckings in the thicker ligaments. On the one hand, the high sessile dislocation density presented in these thinner ligaments provides an additional barrier for dislocation movement, shown in Sec. 3.3. On the other hand, the abundant and uniformly distributed micro neckings/cracks in these thin ligaments help accommodate significant plastic strain without overstressing, which is discussed in detail in Sec. 3.4. Overall, $g1$ exhibits considerably better deformability than $c2$, as illustrated in Fig. 1.

3.3 Dislocation Activities and Plasticity. As mentioned in Sec. 3.2, there are many stacking faults in $c1$ and $g1$, even when there is no external strain. These stacking faults are formed during the relaxation period and are associated with the initial dislocations: the high surface energy of the tortuous structure—especially the thinner ligaments– promotes the nucleation and propagation of Shockley partial dislocations. When the leading partial propagates across the ligament, a layer of stacking faults is formed between the leading and trailing partial. Thus, the stacking fault density is also an indicator of the dislocation density. Our previous work has already demonstrated that dislocation nucleation in NP is closely related to the surface energy [17,37]; the larger the surface energy, the easier it for dislocations to nucleate. The total energy of surface atoms of the $c1$, $c2$, and $g1$ before relaxation are calculated as 290, 86 keV, and 152 keV, respectively. Even when using only atoms that are at least 10 nm away from the box surface to exclude the free surface and sharp edge effect as mentioned in Sec. 2.1, the total energy of surface atoms of $c1$ $c2$ and $g1$ would be 186 keV, 48 keV, and 86 keV. This difference in surface energy is due to the thinner ligaments having a higher surface-to-volume ratio. Figure 4 presents the evolution of Shockley dislocation density [46] and sessile dislocation density [46] as a function of strain during tensile loading. It is observed that both $c1$ and $g1$ have considerably higher initial dislocation density after energy minimization and relaxation than the $c2$. Further examination shows that the dislocations in $g1$ are mostly localized in the area where ligament size is small, and surface energy is high. It is evident that dislocation nucleation is indeed related to surface energy.

These dislocations observed include Shockley partials and sessile dislocations. A large portion of the sessile dislocations is stair-rod dislocations [46,47], which are formed when two Shockley leading partials from different slip planes meet (e.g., $\frac{1}{6}[\bar{1}2\bar{1}] + \frac{1}{6}[1\bar{1}2] =: \frac{1}{3}[\bar{1}2\bar{1}]$). This dislocation structure with two interacting stacking faults and a stair-rod dislocation at its apex is

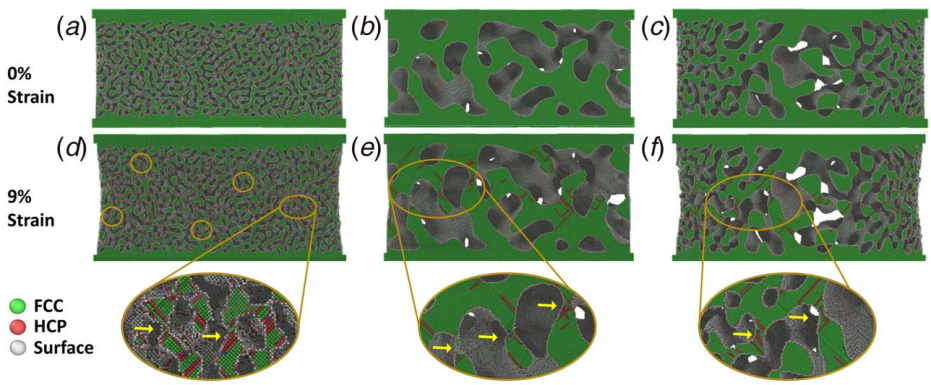

Fig. 3 (*a*)–(*c*) Snapshots of c1, c2, and *g*1 at 0% strain. (*d*)–(*f*) Snapshots of c1, c2, and *g*1 at 9% strain, with magnifications of the circled area showing destabilization. Arrows indicated the exact ligaments that shows necking.

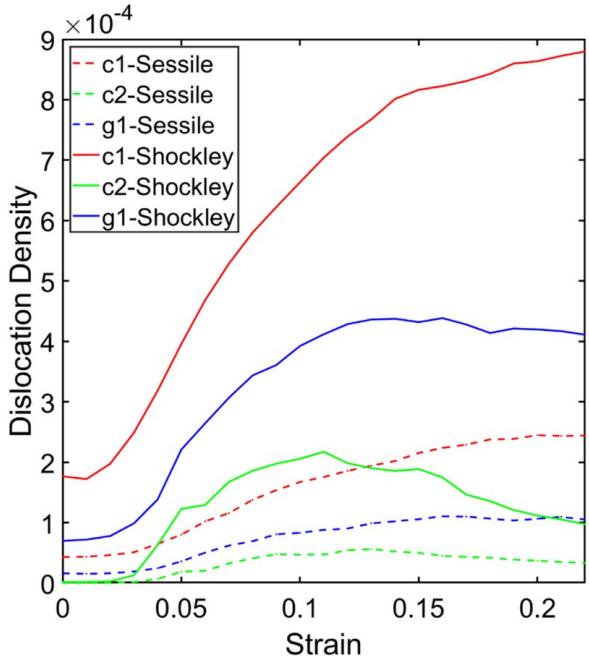

Fig. 4 Evolution of Shockley dislocation density and sessile dislocation density during the loading process. At low external strain (<2.3%), Shockley and sessile dislocation density in c2 is negligible.

also known as a Lomer-Cottrell lock [46]. It has a burgers vector that is not in the slip plane, rendering it sessile and block further mobile dislocation propagation under straining. Thus, any plastic instability associated with mobile dislocation propagation, such as localized necking and failure of ligaments, is postponed in structures with Lomer-Cottrell locks. As a result, structures with Lomer-Cottrell locks can exhibit enhanced strain hardening and ductility [7,17,47]. Thinner ligaments exhibit a much larger surface area and surface stress, which is the driving force for dislocation nucleation, and therefore see a much higher initial dislocation density.

Figure 5 shows the HCP density distribution in the structure at different external strains for $c1$, $c2$, and $g1$. The HCP Cu observed in the structure is mostly stacking faults (i.e., the red atoms in Fig. 3) between the leading and trailing Shockley partials. At 0% strain, the initial stacking faults in $c2$ are uniform across the entire structure without localization. For stacking faults in $c1$ at 0% strain, it is also mostly uniform in the middle but with additional spiking close to the surface, which is due to the relaxation of the sharp edges. As the strain increases, stacking fault distribution will evolve in different patterns. In $c1$, we can see that the distribution remains similar to the 0% curve, but the spiking near the surface intensifies. For $c2$, the distribution reshapes into peaks and valleys, indicating heavily localized deformation: stacking faults are densely concentrated in a handful of areas (peak positions) rather than distributing uniformly in the structure as in $c1$. For the gradient structure, the stacking faults distribution behaves like a combination of $c1$ and $c2$: at 0% strain, it is related to the ligament size—HCP count is around 0.1/nm^3 near the core and increases to around 0.7/nm^3 monotonically to the surface. At high external strain, it is seen that stacking faults is more prominent in two areas due to different mechanisms. First, new peaks are formed in the middle, suggesting the thick ligaments in the middle show similar localized deformation as in $c2$, which is harmful to the deformability. Second, the high sessile dislocation density near the surface blocks dislocation movement and leads to stacking fault buildup. This enhances structure deformability and counteracts the localized plasticity in the middle.

It is noticed that in both the $c1$ and $g1$, the HCP count mostly keeps increasing during straining. However, HCP count in $c2$ increases drastically during the initial stage of loading, but it reaches its peak at around 10% strain, and it starts to decrease afterward. The HCP density reduction (i.e., stacking fault dissipation) is observed to be associated with the necking of ligaments. Due to the lack of obstacles, the Shockley partials move freely in the thick ligaments. When a trailing partial propagates across the entire ligament and exits through the surface, the stacking fault layer between the leading partial and trailing partial will also disappear, leaving a surface step at the exit point. Multiple surface steps occurring close to each other will become necking, and together, they cause crack opening. Such instance of severe necking is rare in $c1$ and $g1$ because the presence of sessile dislocations greatly hindered Shockley partials' movement.

3.4 Strain and Stress Accommodation. Plots of the distributions of shear strain and σ_{zz} for the gradient structure are shown in Fig. 6. At the beginning of the deformation, the stress and shear strain are distributed uniformly along the gradient direction. As the structure is subjected to uniaxial tensile loading, stress is observed to rise in the larger ligament area. The shear strain is observed to increase in the thin ligament area. Notice that this study's uniaxial tension is a uniform deformation different from non-uniform deformation such as bending, torsion, or indentation. But the strain/stress gradient suggests an inhomogeneous response: the contrasting distribution of strain and stress indicates that part of the structure with thin ligaments is able to accommodate a significant amount of strain without developing too much stress when

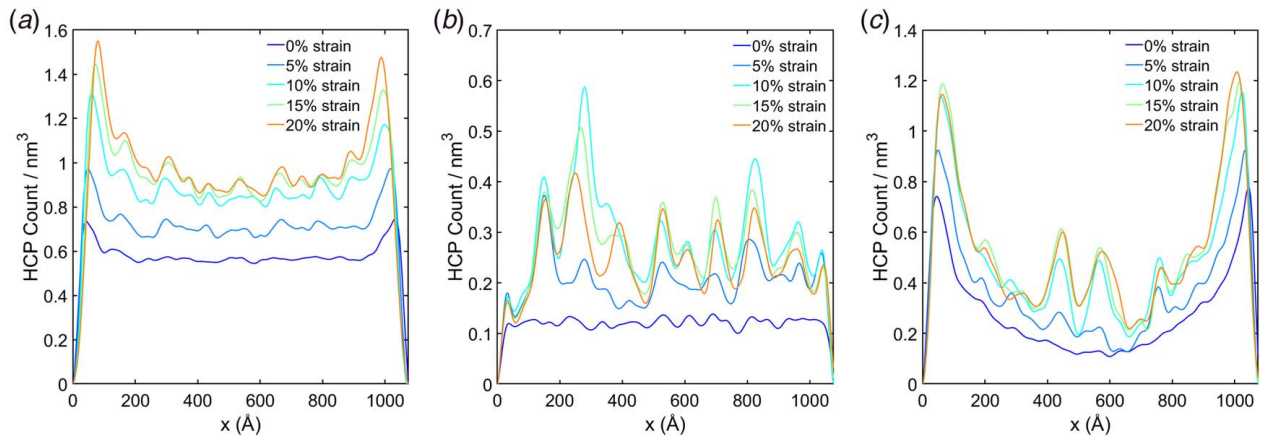

Fig. 5 HCP atom density (i.e., stacking faults density) distribution along the *x*-axis for (*a*) c1 (*b*) c2, and (*c*) *g*1. Curves in different color denote the distribution at different external strain values.

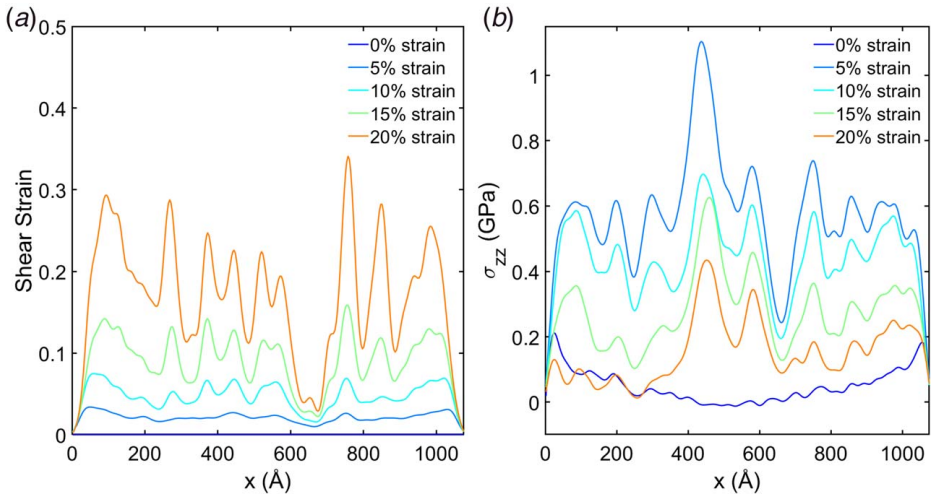

Fig. 6 (*a*) Shear strain and (*b*) σ_zz distribution along the *x*-direction for *g*1. At 20% external strain, shear strain is more localized at the surface and σ_zz is more localized at the core.

under straining. And these thin ligaments are the key to maintain structural integrity under deformation and enhance its ductility accordingly. In contrast, the area closer to the core with a large ligament size, albeit providing superior strength to the entire structure, is softer and more susceptible to necking and crack opening. Thus, a synergy of high strength and good ductility is achieved in the gradient structure.

4 Conclusion

In conclusion, we have successfully generated a new type of NP structure with a ligament size gradient and demonstrated its remarkable mechanical properties. The gradient structure exhibits a similar strength to conventional NP structures with thick ligaments while shows far superior deformability. Thick ligaments in the structure yield at high stress and contribute to the graded structure's exceptional strength. Thin ligaments in the structure promote micro necks that are far away from each other, allowing the structure to deform uniformly. Furthermore, high sessile dislocation density is observed due to the thin ligaments' high surface energy, hindering sessile dislocation movement and allowing enhanced plastic strain accommodation. As a result, graded NP structure shows unprecedented strength and deformability comparing to conventional NP structure with constant ligament size. This study provides a potential method to design an NP structure with exceptional performance and gives new insights regarding the ligament size effect in NP metals.

Acknowledgment

The authors would like to thank Haomin Liu for the discussion and comments. This study was supported by the National Science Foundation (Grant No. 1609587). Computational resources were provided by the Center for Integrated Research Computing at the University of Rochester.

The authors dedicate this article in memory of Hussein Zbib, for his unprecedented contributions to research in the field of 3D dislocation dynamics and defects in metals, multiscale modeling of metal plasticity, and strain gradient plasticity theory.

Conflict of Interest

There are no conflicts of interest.

Data Availability Statement

The data sets generated and supporting the findings of this article are obtainable from the corresponding author upon reasonable request. The authors attest that all data for this study are included in the paper.

References

[1] Bai, Q., Si, C., Zhang, J., and Zhang, Z., 2016, "Sign Inversion of Surface Stress-Charge Response of Bulk Nanoporous Nickel Actuators With Different Surface States," Phys. Chem. Chem. Phys., **18**(29), pp. 19798–19806.
[2] Hu, K., Lan, D., Li, X., and Zhang, S., 2008, "Electrochemical DNA Biosensor Based on Nanoporous Gold Electrode and Multifunctional Encoded DNA−Au Bio Bar Codes," Anal. Chem., **80**(23), pp. 9124–9130.
[3] Biener, J., Wittstock, A., Zepeda-Ruiz, L. A., Biener, M. M., Zielasek, V., Kramer, D., Viswanath, R. N., Weissmuller, J., Baumer, M., and Hamza, A. V., 2009, "Surface-Chemistry-Driven Actuation in Nanoporous Gold," Nat. Mater., **8**(1), pp. 47–51.
[4] Biener, M. M., Biener, J., Wichmann, A., Wittstock, A., Baumann, T. F., Bäumer, M., and Hamza, A. V., 2011, "ALD Functionalized Nanoporous Gold: Thermal Stability, Mechanical Properties, and Catalytic Activity," Nano Lett., **11**(8), pp. 3085–3090.
[5] Seker, E., Reed, M. L., and Begley, M. R., 2009, "Nanoporous Gold: Fabrication, Characterization, and Applications," Materials, **2**(4), pp. 2188–2215.
[6] Biener, J., Hodge, A. M., Hamza, A. V., Hsiung, L. M., and Satcher, J. H., 2005, "Nanoporous Au: A High Yield Strength Material," J. Appl. Phys., **97**(2), p. 024301.
[7] Sun, X. Y., Xu, G. K., Li, X. Y., Feng, X. Q., and Gao, H. J., 2013, "Mechanical Properties and Scaling Laws of Nanoporous Gold," J. Appl. Phys., **113**(2), p. 023505.
[8] Crowson, D., Farkas, D., and Corcoran, S., 2007, "Geometric Relaxation of Nanoporous Metals: The Role of Surface Relaxation," Scr. Mater., **56**(11), pp. 919–922.
[9] Shargh, A. K., Madejski, G. R., McGrath, J. L., and Abdolrahim, N., 2020, "Molecular Dynamics Simulations of Brittle to Ductile Transition in Failure Mechanism of Silicon Nitride Nanoporous Membranes," Mater. Today Commun., **25**(1), p. 101657.
[10] Shargh, A. K., and Abdolrahim, N., 2019, "Molecular Dynamics Simulation of Structural Changes in Single Crystalline Silicon Nitride Nanomembrane," Ceram. Int., **45**(17, Part B), pp. 23070–23077.
[11] Biener, J., Hodge, A. M., Hayes, J. R., Volkert, C. A., Zepeda-Ruiz, L. A., Hamza, A. V., and Abraham, F. F., 2006, "Size Effects on the Mechanical Behavior of Nanoporous Au," Nano Lett., **6**(10), pp. 2379–2382.
[12] Hodge, A. M., Biener, J., Hayes, J. R., Bythrow, P. M., Volkert, C. A., and Hamza, A. V., 2007, "Scaling Equation for Yield Strength of Nanoporous Open-Cell Foams," Acta Mater., **55**(4), pp. 1343–1349.
[13] Crowson, D. A., Farkas, D., and Corcoran, S. G., 2009, "Mechanical Stability of Nanoporous Metals With Small Ligament Sizes," Scr. Mater., **61**(5), pp. 497–499.
[14] Liu, H., and Abdolrahim, N., 2020, "A Modified Scaling Law for Stiffness of Nanoporous Materials Based on Gyroid Cell Model," Int. J. Mech. Sci., **166**(1), p. 105223.
[15] Liu, H., He, L., and Abdolrahim, N., 2018, "Molecular Dynamics Simulation Studies on Mechanical Properties of Standalone Ligaments and Networking

Nodes: A Connection to Nanoporous Material," Modell. Simul. Mater. Sci. Eng., **26**(7), p. 075001.
[16] To, A. C., Tao, J., Kirca, M., and Schalk, L., 2011, "Ligament and Joint Sizes Govern Softening in Nanoporous Aluminum," Appl. Phys. Lett., **98**(5), p. 051903.
[17] He, L., and Abdolrahim, N., 2018, "Deformation Mechanisms and Ductility Enhancement in Core-Shell Cu@Ni Nanoporous Metals," Comput. Mater. Sci., **150**(1), pp. 397–404.
[18] Liu, Z., Meyers, M. A., Zhang, Z., and Ritchie, R. O., 2017, "Functional Gradients and Heterogeneities in Biological Materials: Design Principles, Functions, and Bioinspired Applications," Prog. Mater. Sci., **88**(1), pp. 467–498.
[19] Gao, H., Ji, B., Jäger, I. L., Arzt, E., and Fratzl, P., 2003, "Materials Become Insensitive to Flaws at Nanoscale: Lessons From Nature," Proc. Natl. Acad. Sci. U. S. A., **100**(10), p. 5597–5600.
[20] Ray, A. K., Mondal, S., Das, S. K., and Ramachandrarao, P., 2005, "Bamboo—A Functionally Graded Composite-Correlation Between Microstructure and Mechanical Strength," J. Mater. Sci., **40**(19), pp. 5249–5253.
[21] Lu, K., 2014, "Making Strong Nanomaterials Ductile With Gradients," Science, **345**(6203), p. 1455–1456.
[22] Fang, T. H., Tao, N. R., and Lu, K., 2014, "Tension-Induced Softening and Hardening in Gradient Nanograined Surface Layer in Copper," Scr. Mater., **77**(1), pp. 17–20.
[23] Chen, W., You, Z. S., Tao, N. R., Jin, Z. H., and Lu, L., 2017, "Mechanically-Induced Grain Coarsening in Gradient Nano-grained Copper," Acta Mater., **125**(1), pp. 255–264.
[24] Van der Stok, J., Van der Jagt, O. P., Amin Yavari, S., De Haas, M. F. P., Waarsing, J. H., Jahr, H., Van Lieshout, E. M. M., Patka, P., Verhaar, J. A. N., Zadpoor, A. A., and Weinans, H., 2013, "Selective Laser Melting-Produced Porous Titanium Scaffolds Regenerate Bone in Critical Size Cortical Bone Defects," J. Orthop. Res., **31**(5), pp. 792–799.
[25] Li, X., Lu, L., Li, J., Zhang, X., and Gao, H., 2020, "Mechanical Properties and Deformation Mechanisms of Gradient Nanostructured Metals and Alloys," Nat. Rev. Mater., **5**(9), pp. 706–723.
[26] Liu, F., Mao, Z., Zhang, P., Zhang, D. Z., Jiang, J., and Ma, Z., 2018, "Functionally Graded Porous Scaffolds in Multiple Patterns: New Design Method, Physical and Mechanical Properties," Mater. Des., **160**(1), pp. 849–860.
[27] Wang, Y., Yang, G., Wang, W., Wang, X., Li, Q., and Wei, Y., 2017, "Optimal Stress and Deformation Partition in Gradient Materials for Better Strength and Tensile Ductility: A Numerical Investigation," Sci. Rep., **7**(1), p. 10954.
[28] Ashby, M. F., 1970, "The Deformation of Plastically Non-Homogeneous Materials," Philos. Mag. A, **21**(170), pp. 399–424.
[29] Huang, C. X., Wang, Y. F., Ma, X. L., Yin, S., Höppel, H. W., Göken, M., Wu, X. L., Gao, H. J., and Zhu, Y. T., 2018, "Interface Affected Zone for Optimal Strength and Ductility in Heterogeneous Laminate," Mater. Today, **21**(7), pp. 713–719.
[30] Li, J., Lu, W., Gibson, J., Zhang, S., Chen, T., Korte-Kerzel, S., and Raabe, D., 2018, "Eliminating Deformation Incompatibility in Composites by Gradient Nanolayer Architectures," Sci. Rep., **8**(1), p. 16216.
[31] Cahn, J. W., 1965, "Phase Separation by Spinodal Decomposition in Isotropic Systems," J. Chem. Phys., **42**(1), pp. 93–99.
[32] Soyarslan, C., Bargmann, S., Pradas, M., and Weissmüller, J., 2018, "3D Stochastic Bicontinuous Microstructures: Generation, Topology and Elasticity," Acta Mater., **149**(1), pp. 326–340.
[33] Plimpton, S., 1995, "Fast Parallel Algorithms for Short-Range Molecular Dynamics," J. Comput. Phys., **117**(1), pp. 1–19.
[34] Mishin, Y., Mehl, M. J., Papaconstantopoulos, D. A., Voter, A. F., and Kress, J. D., 2001, "Structural Stability and Lattice Defects in Copper: Ab Initio, Tight-Binding, and Embedded-Atom Calculations," Phys. Rev. B, **63**(22), p. 224106.
[35] Mastorakos, I. N., Abdolrahim, N., and Zbib, H. M., 2010, "Deformation Mechanisms in Composite Nano-layered Metallic and Nanowire Structures," Int. J. Mech. Sci., **52**(2), pp. 295–302.
[36] He, L., and Abdolrahim, N., 2019, "Stress-Assisted Structural Phase Transformation Enhances Ductility in Mo/Cu Bicontinuous Intertwined Composites," ACS Appl. Nano Mater., **2**(4), pp. 1890–1897.
[37] He, L., Hadi, M., Liu, H., and Abdolrahim, N., 2020, "Mechanism of Coarsening and Deformation Behavior of Nanoporous Cu With Varying Relative Density," J. Mater. Res., **35**(19), pp. 2620–2628.
[38] Neogi, A., He, L., and Abdolrahim, N., 2019, "Atomistic Simulations of Shock Compression of Single Crystal and Core-Shell Cu@Ni Nanoporous Metals," J. Appl. Phys., **126**(1), p. 015901.
[39] Stukowski, A., 2009, "Visualization and Analysis of Atomistic Simulation Data With OVITO–The Open Visualization Tool," Modell. Simul. Mater. Sci. Eng., **18**(1), p. 015012.
[40] Larsen, P. M., Schmidt, S., and Schiøtz, J., 2016, "Robust Structural Identification via Polyhedral Template Matching," Modell. Simul. Mater. Sci. Eng., **24**(5), p. 055007.
[41] Stukowski, A., Bulatov, V. V., and Arsenlis, A., 2012, "Automated Identification and Indexing of Dislocations in Crystal Interfaces," Modell. Simul. Mater. Sci. Eng., **20**(8), p. 085007.
[42] Hart, E. W., 1967, "Theory of the Tensile Test," Acta Metall., **15**(2), pp. 351–355.
[43] Hutchinson, J. W., and Neale, K. W., 1977, "Influence of Strain-Rate Sensitivity on Necking Under Uniaxial Tension," Acta Metall., **25**(8), pp. 839–846.
[44] Yasnikov, I. S., Vinogradov, A., and Estrin, Y., 2014, "Revisiting the Considère Criterion From the Viewpoint of Dislocation Theory Fundamentals," Scr. Mater., **76**(1), pp. 37–40.
[45] Zhu, Y. T., and Wu, X. L., 2018, "Ductility and Plasticity of Nanostructured Metals: Differences and Issues," Mater. Today Nano, **2**(1), pp. 15–20.
[46] Hull, D., and Bacon, D. J., 2011, *Introduction to Dislocations*, 5th ed., Vol. 1, Butterworth-Heinemann, Oxford.
[47] Martínez, E., and Uberuaga, B. P., 2015, "Mobility and Coalescence of Stacking Fault Tetrahedra in Cu," Sci. Rep., **5**(1), p. 9084.